DOI: https://doi.org/10.53256/COSE_240101

# Influence of Permeability and Wave Steepness on Wave Forces on Crown Walls for Non-Breaking Waves

M. R. Eldrup[a,*], T. Lykke Andersen[a], J. Molines[b] and J. Q. H. Nørgaard[c]
[a]*Department of the Built Environment, Aalborg University, Denmark*
[b]*Universitat Politècnica de València – Research Institute of Transportation and Territory, Spain*
[c]*Coastal Department, Niras, Denmark*

[*]*Department of the Built Environment, Thomas Manns Vej 23, 9220 Aalborg Ø, Denmark, mrel@build.aau.dk*

ABSTRACT: This study investigates how structural permeability and wave steepness affect wave-induced loads on crown walls in rubble mound breakwaters. Evaluating prediction models by Nørgaard et al. (2013) and Molines et al. (2018) against measurements from 591 new physical model tests at Aalborg University revealed that the permeability has minimal impact on the horizontal forces, while influencing significantly the vertical loads and the overturning moment. Nørgaard et al. (2013) and Molines et al. (2018) formulae provide similar agreement against the experimental data for horizontal forces. The Nørgaard et al. (2013) formula is more accurate for predicting base pressures and vertical forces. Both prediction methods show varying accuracy depending on the conditions. The experimental data shows significantly less variation in repetition tests than predicted by the formulae, indicating that further improvements of the formulae can be achieved in future work.

## 1 INTRODUCTION

Rubble mound structures protect harbours or the hinterland from the sea, with wave overtopping as a key design criterion. The height of the structure is determined by the allowable wave overtopping. Crown walls are commonly incorporated into rubble mound structures to provide a service road on top of the structure, and they may also be used to reduce wave overtopping.

Several studies have investigated wave-induced loads on crown walls; see Pedersen (1996), Martin et al. (1999), Nørgaard et al. (2013), and Molines et al. (2018).

Nørgaard et al. (2013) expanded the applicability of the Pedersen (1996) formulae to depth-limited waves where the wave height distributions might deviate significantly from the Rayleigh distribution. They noted that their formulae may yield unrealistic results for waves with steepness $H_{m0}/L_{m0} < 0.018$, with $H_{m0}$ being the spectral wave height and $L_{m0} = T_m^2 g/(2\pi)$ being the deep-water wavelength calculated with the mean period from zero down crossings at the toe of the structure. Furthermore, they did not test the impact of different structural permeabilities, leaving the applicability of their findings to impermeable structures uncertain.

Molines et al. (2018) conducted tests with wave steepness defined as $H_{m0}/L_{m-1,0} > 0.011$ with $L_{m-1,0} = T_{-1,0}^2 g/(2\pi)$, which slightly expanded the database compared to the work by Nørgaard et al. (2013). However, the effects of very low wave steepness remain unexplored. Additionally, Molines et al. (2018) only examined permeable structures, leaving the applicability of their findings to impermeable structures untested.

The purpose of the present study is thus to investigate the influence of structure permeability and wave steepness on crown wall loading. Waves of lower steepness than those tested previously are also included. The new data is compared against existing formulae. For that purpose, 591 new model tests on rock-armoured mound breakwaters have been conducted at Aalborg University.

First, the formulae by Nørgaard et al. (2013) and Molines et al. (2018) are described, followed by the setup and analysis of new physical model tests. Uncertainties from wave train realisation and armour placement are then examined, before conclusions are drawn and the effects of wave steepness, permeability, and deviations from the formulae are discussed.

## 2 EXISTING PREDICTION METHODS FOR WAVE LOADS

### 2.1 *Nørgaard et al. (2013)*

Nørgaard et al. (2013) found that the original formulae by Pedersen (1996) provided reliable estimates of wave-induced loads for non-breaking waves on the foreshore and when armour units fully protected the crown wall. However, for partially unprotected walls and under shallow-water conditions, the loads were found to be overpredicted. Nørgaard et al. (2013) conducted 162 physical model tests on a rock-armoured structure with a front slope of 1:1.5 and a foreshore slope of 1:98.

To characterise the permeability of the tested structure in the present study, the notional permeability defined by Van der Meer (1988) is adopted. Based on the method developed by Eldrup et al. (2019), the notional permeability is estimated as $P \approx 0.4$. The tests consisted of approximately 1,250 waves per test, and the incident wave conditions were generated using a JONSWAP spectrum with a peak enhancement factor of $\gamma = 3.3$. Pressures were sampled at 1,500 Hz and subsequently digitally low-pass filtered to obtain an effective sampling frequency consistent with the spatial resolution of the pressure transducers and the celerity of the peak pressures. A cut-off frequency of 250 Hz was applied.

Nørgaard et al. (2013) also included data from Pedersen (1996), who tested structures with front slopes of 1:1.5, 1:2.5, and 1:3.5. The notional permeability of these structures is estimated to be $P \approx 0.2$. In those tests, the generated waves were likewise based on a JONSWAP spectrum with a peak enhancement factor of 3.3.

Nørgaard et al. (2013) extended the applicability of the original formulae to shallow-water conditions. These modifications included the use of $H_{0.1\%}$ in the run-up formulation, replacing $H_{1/3}$, following the approach proposed by Van der Meer and Stam (1992). In addition, the expressions for slamming pressures acting on the unprotected section of the crown wall and for the overturning moment induced by horizontal wave forces were revised.

The original formulae by Pedersen (1996) for horizontal wave loads, which were also adopted by Nørgaard et al. (2013), are given in Eq. (1). Compared with the original formulation by Pedersen (1996), the mean value ($\mu$) of coefficient $b$and the standard deviations ($\sigma$) of coefficients $a$and $b$were updated.

$$
\begin{aligned}
F_{H,0.1\%} &= F_{Hu,0.1\%} + F_{Hl,0.1\%} \\
F_{Hu,0.1\%} &= a\sqrt{\frac{L_{m0}}{G_c}}\, p_m y_{eff} b \\
F_{Hl,0.1\%} &= \frac{1}{2} a\sqrt{\frac{L_{m0}}{G_c}}\, p_m V h_{prot} \\
p_m &= g\rho_w(\mathrm{R}_{u,0.1\%} - A_c) \\
\mathrm{y_{eff}} &= \min\left(\frac{y}{2}, f_c\right) \\
V &= \min\left(\frac{V_2}{V_1}, 1\right)
\end{aligned}
\tag{1}
$$

Here, $F_{\mathrm{H},0.1\%}$ denotes the horizontal force exceeded by 0.1% of the waves. $F_{Hu,0.1\%}$ and $F_{Hl,0.1\%}$ represent the horizontal forces acting on the unprotected and protected parts of the wall, respectively. The mean values and standard deviations of coefficients $a$and $b$ are provided in Table 1. $G_\mathrm{c}$ denotes the horizontal width of the armour crest, and $A_\mathrm{c}$ is the armour crest freeboard. $p_\mathrm{m}$ represents the stagnation pressure, and $y$ is the vertical run-up wedge thickness at the intersection between the front slope and the horizontal crest. $f_\mathrm{c}$ is the height of the unprotected part of the wall, and $h_\mathrm{prot}$ is the height of the protected part of the wall. $y_\mathrm{eff}$ denotes the effective impact zone on the unprotected wall. $V_1$ and $V_2$ are illustrated in Fig. 1. $R_\mathrm{u,01\%}$ represents the (fictitious) 0.1% exceedance value for the wave run-up, obtained by assuming an infinitely long slope. All geometric parameters are illustrated in Fig. 1.

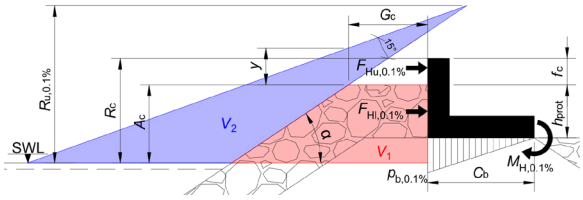


Figure 1. Parameters used in the formulae proposed by Nørgaard et al. (2013) .

The run-up formula originally proposed by Van der Meer and Stam (1992) and reformulated by Nørgaard et al. (2013) is given in Eq. (2). The formulation is subject to an upper limit of $1.388H_{0.1\%}$.

$$
\begin{aligned}
\mathrm{R}_{u,0.1\%} &= \begin{cases} 0.603 H_{0.1\%}\xi_{\mathrm{m0}}, & \xi_{\mathrm{m0}} \le 1.5 \\ 0.722 H_{0.1\%}\xi_{\mathrm{m0}}^{0.55}, & \xi_{\mathrm{m0}} > 1.5 \end{cases} \\
\xi_{\mathrm{m0}} &= \frac{\tan(\alpha)}{\sqrt{H_{1/3}/L_{m0}}}
\end{aligned}
\tag{2}
$$

Nørgaard et al. (2013) also revised the formulation of the horizontal contribution to the overturning moment at the heel of the crown wall, as expressed in Eq. (3).

$$
\begin{aligned}
\mathrm{M}_{H,0.1\%} = F_{Hu,0.1\%}&\left(h_{prot} + \frac{1}{2} y_{eff}\, e_2\right) \\
&+ F_{Hl,0.1\%}\frac{1}{2} h_{prot} e_1
\end{aligned}
\tag{3}
$$

The mean values and standard deviations of coefficients $e_1$and $e_2$are provided in Table 1.

The vertical force acting on the base slab is calculated from the pressure at the front corner, assuming a triangular pressure distribution with zero pressure at the heel. Accordingly, the vertical force can be calculated using Eq. (4).

$$P_{b,01\%} = d\,V\,p_m$$
$$F_{V,0.1\%} = P_{b,01\%}\frac{1}{2}\,C_b \quad (4)$$

where $C_b$ denotes the horizontal length of the base slab, as shown in Fig. 1. The mean value and standard deviation of coefficient $d$ are given in Tab. 1.

Table 1. μ and σ of the coefficients used in the formulae by Nørgaard et al. (2013).

| | ***a*** | ***b*** | ***d*** | ***e*₁** | ***e*₂** |
|---|---|---|---|---|---|
| μ | 0.21 | 1 | 1 | 0.95 | 0.4 |
| σ | 0.06 | 0.81 | 0.41 | 0.53 | 0.78 |

Assuming normally distributed uncertainty, the 90% confidence interval of the formulae may be estimated as $\mu \pm 1.64\sigma$, based on the values reported in Table 1.

Nørgaard et al. (2013) observed that $F_{H,0.1\%}$ does not necessarily occur simultaneously with $P_{b,0.1\%}$. Consequently, applying the maximum horizontal and vertical forces concurrently is expected to lead to overestimation of the destabilising forces. The overturning moment $M_{H,0.1\%}$ was found to be highly correlated with the moment at the instant of maximum horizontal force.

### 2.2 *Molines et al. (2018)*

Molines et al. (2018) used 163 experimental tests from Molines (2016) together with 111 tests from Pedersen (1996) to derive new empirical formulae for predicting wave-induced forces acting on crown walls. The tests presented in Molines (2016) comprised breakwaters with a 1:1.5 front slope, armoured with either Cubipods® in one or two layers, or with cubes in two layers. The notional permeability of these structures is estimated to range between $P \approx 0.2$ and $P \approx 0.4$. The foreshore was horizontal in all tests. The generated waves followed a JONSWAP spectrum with peak enhancement factors of 1.0 or 3.3 and had a duration of approximately 1,000 waves. The sampling frequency was 20 Hz.

Several formulae were developed using only the average wave overtopping discharge, $q$, as input, while other formulations included additional geometric and wave parameters. For the purpose of the present comparison, only the equations based solely on the average overtopping discharge are considered. These are presented in Eq. (5).

$$Fh = \frac{F_{H,0.1\%}}{0.5\rho g C_h^2} = c_1 + 0.6\log(Q)$$
$$Pb = \frac{P_{b,0.1\%}}{0.5\rho g C_h} = c_2 + 0.52\log(Q) \quad (5)$$
$$Mh = \frac{M_{H,0.1\%}}{\rho g C_h^3} = c_3 + 0.11\log(Q)$$

where $F_h$, $P_b$, and $M_h$ denote the dimensionless horizontal force, the base pressure at the lower front corner, and the horizontal overturning moment exceeded by 0.1% of the waves, respectively. $C_h$ is the height of the crown wall, and $Q$ is the dimensionless average overtopping discharge, defined as $q/(gH_{m0}^3)^{0.5}$. $c_1$, $c_2$ and $c_3$ are fitting parameters, with mean values and standard deviations provided in Table 2. The remaining parameters are illustrated in Fig. 2.

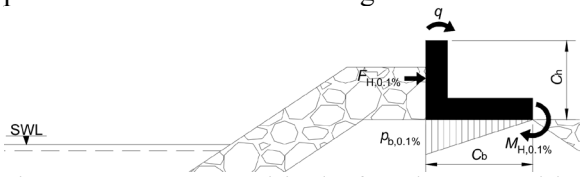


Figure 2. Parameters used in the formulae proposed by Molines et al. (2018).

Table 2. μ and σ values of the coefficients used in the formulae by Molines et al. (2018).

| | ***c*₁** | ***c*₂** | ***c*₃** |
|---|---|---|---|
| μ | 3.6 | 4.3 | 0.7 |
| σ | 0.38 | 0.45 | 0.09 |

Regarding the vertical force, assumptions similar to those adopted by Nørgaard et al. (2013) are applied, namely a triangular pressure distribution acting on the base slab. This allows the calculation of both the vertical force and the vertical contribution to the overturning moment about the heel.

Molines et al. (2018) employed the measured average overtopping discharge obtained from the experiments. In cases where these measurements are unavailable, several empirical overtopping formulae were proposed. In the present study, the method developed by Eldrup et al. (2022) is applied to estimate the average overtopping discharge. A comparison between the estimated and measured overtopping discharges is presented in Section 3.2.

## 3 NEW EXPERIMENTAL DATA

### 3.1 *Flume layout and test methodology*

A total of 591 small-scale physical model tests were conducted to investigate a wide range of sea state conditions, water levels, and breakwater cross-sections with varying structural permeability. The experiments were carried out at Aalborg University in the Ocean and Coastal Engineering wave flume. The flume features an

active test section, extending from the mean position of the wavemaker to the start of the passive absorption zone, with dimensions of 15 m × 1.5 m × 1.5 m (length × width × height). All tests were performed over a horizontal bathymetry.

Long-crested irregular waves were generated using the second-order wavemaker theory proposed by Schäffer (1996), incorporating the modifications suggested by Eldrup and Lykke Andersen (2019a). For sea states for which the applicability criteria of Eldrup and Lykke Andersen (2019a) indicated that second-order theory was unsuitable, the ad hoc unified wavemaker approach proposed by Zhang et al. (2007) was applied. The input conditions for this method were derived from simulations performed with the Celeris model developed by Tavakkol and Lynett (2017), a numerical Boussinesq-type wave model. For all sea states, the target wave spectrum was defined using a JONSWAP spectrum with a peak enhancement factor of 3.3. Active wave absorption at the wavemaker, effective for both linear and nonlinear waves, was employed throughout the test programme (Lykke Andersen et al. (2016), (2018)). Wave generation and control were managed using the AwaSys 7 software developed by Aalborg University (2023a). Surface elevations were measured using resistance-type wave gauges manufactured by VTI. A total of 11 wave gauges were installed along the flume; however, only the seven gauges closest to the breakwater were used to estimate the incident wave conditions. Incident and reflected wave components were separated using the method described by Eldrup and Lykke Andersen (2019b). All wave data processing and analysis were performed using the WaveLab software developed by Aalborg University (2023b).

The duration of each test was adjusted according to the sea state, such that approximately 2,000 waves were generated in order to obtain reliable estimates of low exceedance wave loads. The experimental programme included six different target peak wave steepness values, $s_{0p}$, defined using the deep-water wavelength calculated from the peak period $T_p$and the spectral significant wave height $H_{m0}$. The selected peak wave steepness values were $s_{0p} = 0.005$, 0.007, 0.010, 0.020, 0.030, and 0.045. This corresponds to a range of $H_{m0}/L_{m0}$between 0.007 and 0.057, and $H_{m0}/L_{m-1,0}$between 0.005 and 0.050. Non-breaking wave heights in the range $H_{m0} = 0.06$–0.14 m were generated, depending on the stability constraints of the tested structures.

### 3.2 *Tested breakwaters*

Breakwaters with front slopes of 1:1.5 and 1:3 were tested at three different water levels, both with and without an unprotected section of the crown wall. Not all possible combinations of slope, water level, and wall configuration were investigated.

Figure 3 illustrates the geometrical dimensions of the tested breakwaters together with the corresponding tested water levels. Tests including a detachable section of the crown wall—i.e. with armour placed below the wall crest—were conducted at a water level of 86 mm. Tests without this detachable section, corresponding to configurations in which the armour crest and the crown wall crest were at the same elevation, were performed at water levels of 0 mm and 42 mm.

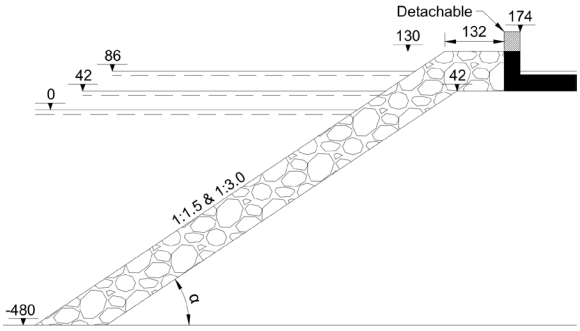


Figure 3. Breakwater dimensions and tested water levels. Measurements are given in millimetres at model scale.

Five different layer compositions were tested, as shown in Fig. 5. The majority of the experiments were carried out on the least permeable (Model A) and the most permeable (Model E) cross-sections, corresponding to notional permeability values of $P = 0.1$and $P = 0.5$, respectively, as defined by Van der Meer (1988). The notional permeability of the remaining cross-sections was estimated. In addition to Model A, an impermeable structure with a thicker filter layer and an estimated notional permeability of $P \approx 0.2$was tested (Model B). A structure with an estimated permeability of $P \approx 0.4$was also examined (Model D), as well as another structure with $P \approx 0.4$but incorporating a slightly finer core material than that proposed Van der Meer (1988) (Model C). Most tests were conducted with a fully protected crown wall ($R_c = A_c$), while a smaller subset of tests included crown walls that were not fully covered by rock armour ($R_c > A_c$).

Models A and E with a front slope of 1:1.5 were each tested six times, with the armour layer rebuilt prior to each test in order to assess the influence of armour stone placement and random

orientation. The same procedure was applied for the 1:3 front slope, although only three repetitions were performed for Model A and two for Model E. In addition, Model E with a front slope of 1:1.5 was tested using five different realisations of the wave train without rebuilding the armour layer, to investigate the influence of wave train variability.

Table 3. Range of tested conditions measured for each model.

| Model | cot(α) | $H_{m0}/L_{m-1,0}$ | $H_{m0}/h$ | $h/L_{m-1,0}$ | $R_c/H_{m0}$ |
|---|---|---|---|---|---|
| A | 1.5 | 0.005-0.050 | 0.10-0.23 | 0.02-0.46 | 0.84-1.95 |
| A | 3.0 | 0.005-0.050 | 0.11-0.30 | 0.02-0.43 | 0.69-1.55 |
| B | 1.5 | 0.005-0.049 | 0.10-0.22 | 0.02-0.46 | 0.88-1.72 |
| C | 1.5 | 0.005-0.049 | 0.11-0.26 | 0.02-0.43 | 0.88-1.53 |
| D | 1.5 | 0.005-0.049 | 0.10-0.26 | 0.02-0.46 | 0.86-1.55 |
| E | 1.5 | 0.005-0.049 | 0.11-0.26 | 0.02-0.43 | 0.88-1.56 |
| E | 3.0 | 0.005-0.049 | 0.15-0.26 | 0.02-0.32 | 0.80-1.54 |

Figure 4 presents a comparison between measured average overtopping discharges and predictions obtained using the method proposed by Eldrup et al. (2022). The results indicate no significant differences in dimensionless average overtopping among the investigated cross-sections. Consequently, a roughness factor of $\gamma_f = 0.40$is adopted for all tested configurations. Nevertheless, further research is required to quantify the detailed influence of structural permeability on the average overtopping discharge.

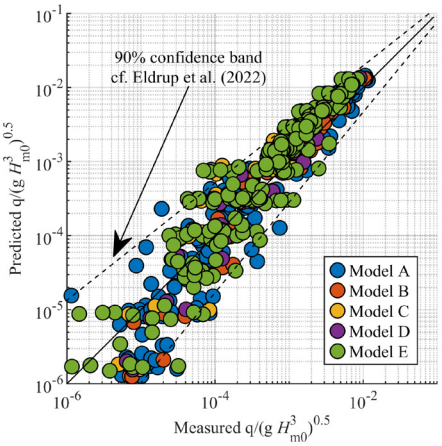


Figure 4. Comparison between measured average overtopping discharge and predictions by Eldrup et al. (2022), applying $\gamma_f = 0.40$.

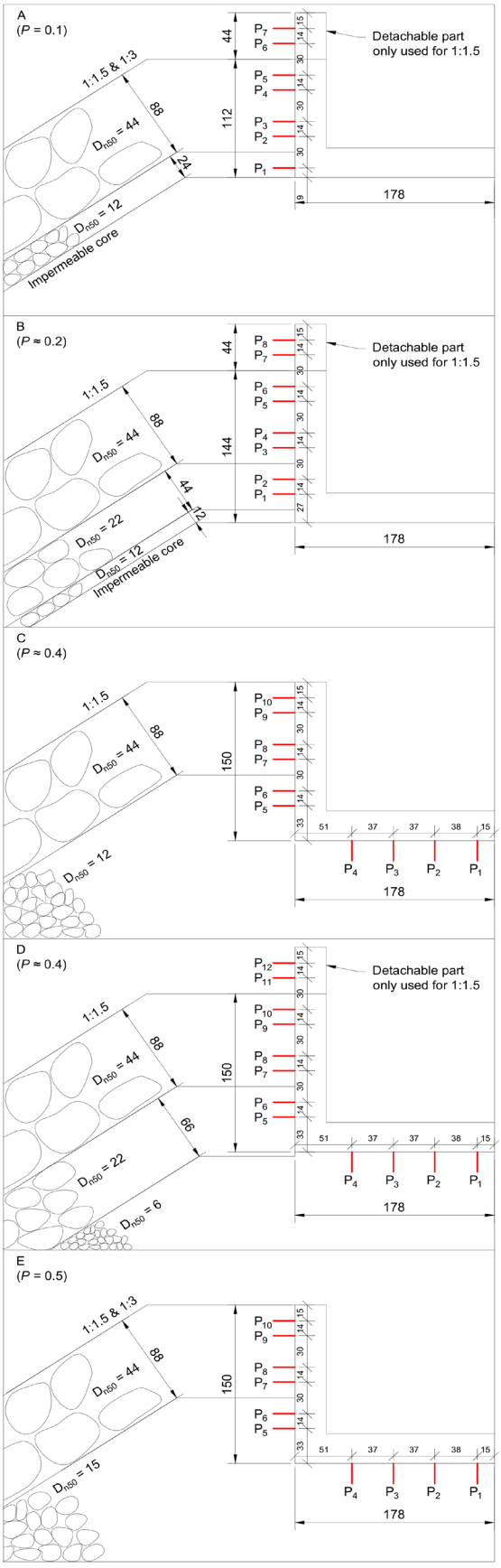


Figure 5. Layer composition of the tested breakwaters and crown wall configurations. Measurements are given in millimetres at model scale. Red lines indicate the locations of pressure transducers.

### 3.3 *Wall layout*

Depending on the tested breakwater configuration, between 10 and 24 Drück PMP UNIK pressure transducers with flush-mounted membranes were used to measure the pressure distribution acting on the crown wall. The pressure transducers were arranged in two adjacent vertical sections, allowing two sensors to be installed at each elevation. This configuration provides measurement redundancy and accounts for variability associated with armour stone placement. The locations of the transducers in both the fixed wall and the detachable wall sections are illustrated in Fig.5 for a representative column. The transducers have a diameter of 20 mm and a frequency response of up to 5 kHz.

### 3.4 *Load analysis*

In the present experiments, pressures were sampled at a frequency of 1,000 Hz. To reduce high-frequency noise and spurious pressure spikes, a moving-average filter was applied to the pressure time series, following the approach described by Lamberti et al. (2011). The smoothing window was fixed at 0.01 s for all tests. This filtering procedure effectively attenuates rapid fluctuations while preserving the impulsive pressure components of the signal.

A median filter was subsequently applied to minimise the effects of slow signal drift, using a window size of 20 s. In addition, the median filter removes the hydrostatic pressure component in tests where the transducers were fully submerged, thereby isolating the wave-induced pressure in the measurements. The combined effect of the two filtering procedures is illustrated in Fig. 6.

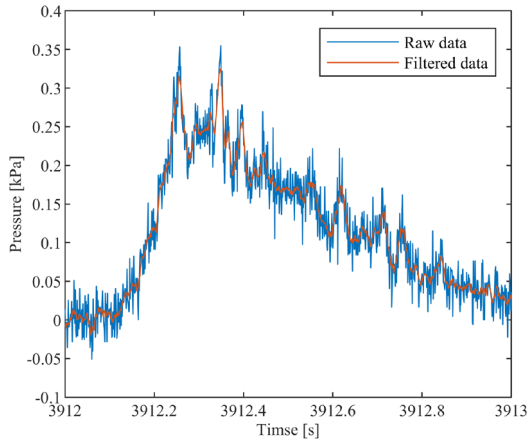


Figure 6. Example of pressure time series recorded by a single transducer before and after filtering.

The filtered pressure values were extrapolated to the edges of the crown wall, and a linear pressure variation was assumed between adjacent transducers. The resulting pressure distributions were then integrated to determine the forces and moments acting on the crown wall. The analysis procedure adopted in the present study is identical to that used by Nørgaard et al. (2013).

## 4 UNCERTAINTY RELATED TO SEA STATE REALISATION

The influence of wave train realisation is illustrated in Fig. 7. Six different random wave seeds were used to generate distinct sea state realisations, each comprising approximately 2,000 waves. The tests were performed on Model E with a front slope of 1:1.5. The selected wave conditions were chosen such that the estimated damage to the armour layer, calculated according to Van der Meer (1988), satisfied $S_d < 1$. This ensured that rearrangement of the armour layer was limited and did not influence the experimental results. The applied significant wave height was $H_{m0} = 0.08$m, and the water level was set to 0 mm.

The figure presents subplots of the dimensionless horizontal wave force, the base pressure at the lower front corner, the 0.1% exceedance wave height $H_{0.1\%}$, and the spectral significant wave height $H_{m0}$. Solid lines indicate model predictions together with their associated 90% confidence bands. While $H_{0.1\%}$ exhibits noticeable variability between different realisations, $H_{m0}$ remains relatively stable, leading to differences in the predicted wave-induced loads.

For the horizontal force, the experimental data fall within the confidence bands of both prediction methods, although the confidence band associated with Molines et al. (2018) is noticeably wider. On average, the formulation by Nørgaard et al. (2013) underpredicts the measured horizontal forces by approximately 25%, whereas the formulation by Molines et al. (2018) overpredicts them by approximately 40%, with the experimental data showing closer agreement with the predictions of Nørgaard. For the base pressure at the lower front corner, both prediction methods overestimate the measured values. The formulation by Nørgaard et al. (2013) overpredicts the base pressure by approximately 50%, although the measurements remain within its 90% confidence interval. In contrast, the formulation by Molines et al. (2018) overpredicts the base pressure by approximately 150%, with the measurements lying outside the

corresponding confidence band. Both models reproduce the general trend of increasing load with decreasing wave steepness; however, the experimental data are systematically shifted relative to the mean model predictions.

Tab. 4 presents the coefficient of variation ($\sigma/\mu$) for both the experimental data and the corresponding model predictions shown in Fig. 7. The variability observed in the experimental data is small compared with the width of the confidence bands associated with the prediction formulae. This suggests that the uncertainty of the prediction methods primarily originates from factors other than wave train realisation. With approximately 2,000 waves per test, the duration of the experiments is therefore considered sufficient to assess the influence of wave steepness and structural permeability.

Table 4. Coefficient of variation ($\sigma/\mu$) for experimental data and prediction formulae shown in Fig. 7.

| $s_{m-1,0}$ | 0.048 | 0.036 | 0.024 | 0.012 | 0.008 | 0.006 |
|---|---|---|---|---|---|---|
| $Fh_{data}$ | 0.06 | 0.11 | 0.03 | 0.07 | 0.07 | 0.06 |
| $Fh_{Molines}$ | 0.40 | 0.30 | 0.25 | 0.20 | 0.18 | 0.17 |
| $Fh_{Nørgaard}$ | 0.29 | 0.29 | 0.29 | 0.29 | 0.29 | 0.29 |
| $Pb_{data}$ | 0.06 | 0.06 | 0.03 | 0.05 | 0.03 | 0.02 |
| $Pb_{Molines}$ | 0.22 | 0.20 | 0.18 | 0.16 | 0.15 | 0.15 |
| $Pb_{Nørgaard}$ | 0.41 | 0.41 | 0.41 | 0.41 | 0.41 | 0.41 |

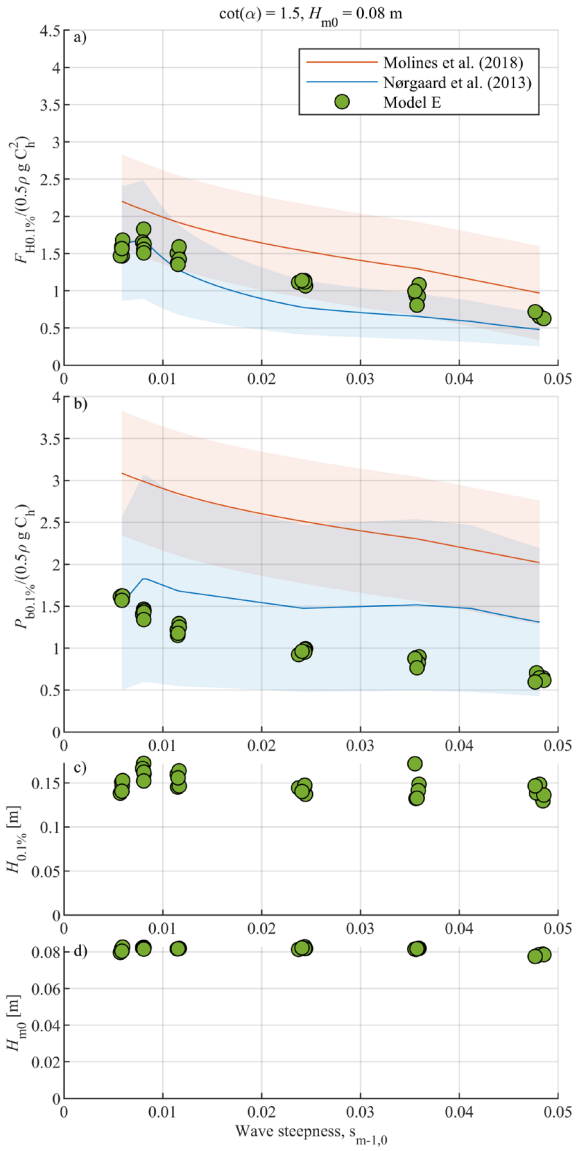


Figure 7. Influence of different wave train realisations on measured and predicted loads. Wave heights are given at model scale.

## 5 UNCERTAINTY RELATED TO RANDOM ARMOUR PLACEMENT

The influence of random armour placement is illustrated in Fig. 8. Experiments involving random positioning and orientation of the armour stones were conducted through six independent rebuilds of the armour layer and are analysed here for Model E with a front slope of 1:1.5. The influence of armour placement is important because pressure transducers may be fully, partially, or not covered by armour stones, thereby affecting the measured pressure signals. Rearrangement of the rubble mound, and consequently the pore structure in front of the crown wall, is therefore conceptually similar to

altering the relative position of the pressure transducers. This effect is particularly relevant when the characteristic size of the armour stones is large compared with the diameter of the pressure transducers.

As the number of pressure transducers increases, the mean load estimates are derived from a larger set of measurements, and the influence of local variations in armour placement is expected to diminish.

Figure 8 presents the dimensionless horizontal force and base pressure together with the corresponding wave heights, in a manner analogous to Fig. 7. The results show values comparable to those observed in Fig. 7 , although with a slightly increased scatter. Nevertheless, the conclusions drawn from the analysis of Fig. 7 also apply to the observations presented in Fig. 8.

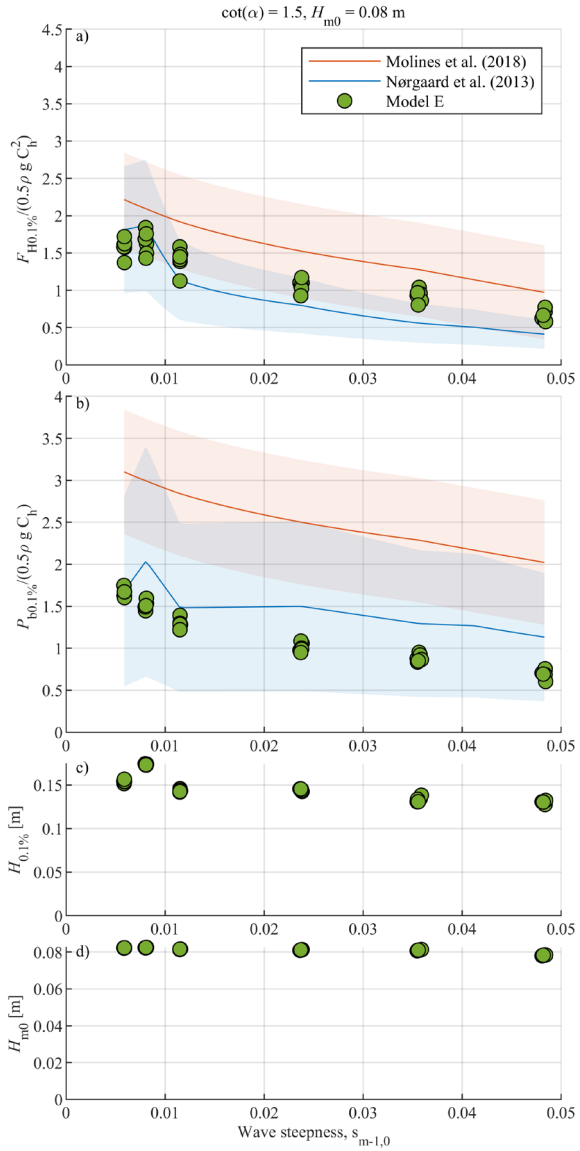


Figure 8. Influence of random armour placement on measured and predicted loads. Wave heights are given at model scale.

Tab. 5 summarises the coefficients of variation ($\sigma/\mu$) for both the experimental data and the prediction formulae illustrated in Fig. 8. Similar to the influence of wave train realisation, the variability observed in the experimental data is significantly smaller than that predicted by the empirical formulae. This indicates that the uncertainty associated with random armour placement is minor compared with the overall uncertainty inherent in the prediction methods. It is therefore concluded that the spatial resolution and number of pressure transducers are sufficient to reliably capture the effects of wave steepness and structural permeability.

Table 5. Coefficient of variation ($\sigma/\mu$) for experimental data and prediction formulae shown in Fig. 8.

| $s_{m-1,0}$ | 0.048 | 0.036 | 0.024 | 0.012 | 0.008 | 0.006 |
|---|---|---|---|---|---|---|
| $Fh_{data}$ | 0.11 | 0.09 | 0.08 | 0.11 | 0.10 | 0.07 |
| $Fh_{Molines}$ | 0.39 | 0.30 | 0.25 | 0.20 | 0.18 | 0.17 |
| $Fh_{Nørgaard}$ | 0.29 | 0.29 | 0.29 | 0.29 | 0.29 | 0.29 |
| $Pb_{data}$ | 0.08 | 0.05 | 0.05 | 0.05 | 0.04 | 0.03 |
| $Pb_{Molines}$ | 0.22 | 0.20 | 0.18 | 0.16 | 0.15 | 0.15 |
| $Pb_{Nørgaard}$ | 0.41 | 0.41 | 0.41 | 0.41 | 0.41 | 0.41 |

Uncertainty associated with armour placement and wave train realisation has a smaller influence on the base pressure than on the horizontal force, as reflected by the lower coefficients of variation. Consequently, the vertical force is also less sensitive to these sources of uncertainty than the horizontal force.

## 6 INFLUENCE OF CORE PERMEABILITY WITH A FULLY PROTECTED WALL

Fig. 9 illustrates the effect of breakwater core permeability on wave-induced loads. The characteristic crown wall heights, $C_h$, are 112 mm for Model A, 144 mm for Model B, and 150 mm for the remaining structures; the latter value is also adopted in the formulae proposed by Nørgaard et al. (2013). Model A, which has an impermeable core, exhibits the highest non-dimensional horizontal forces, although it also has the smallest value of $C_h$. Model B, which is likewise impermeable but has a wall height comparable to the other structures, shows horizontal force levels similar to those of the permeable configurations.

For models with comparable wall heights, the magnitudes of the horizontal forces are nearly identical, indicating that core permeability has a negligible influence on the horizontal wave load. Instead, the results suggest that normalisation with $C_h^2$ is not fully appropriate, as the measured pressure distributions deviate from the assumed

triangular shape. Since the use of smaller $C_h$ values in the formulation by Nørgaard et al. (2013) results in larger non-dimensional forces—consistent with the experimental observations—the wall height is more appropriately represented in the formulation by Nørgaard et al. (2013) than in that of Molines et al. (2018). The fundamental difference between the two approaches lies in the assumed pressure distribution: Nørgaard et al. (2013) adopt a rectangular distribution, whereas Molines et al. (2018) assume a triangular distribution.

A similar conclusion regarding the assumed pressure distribution can be drawn for the base pressure (see Fig 9b), as Model A yields larger values than the remaining structures. Nevertheless, an effect of core permeability can be observed, as Model B tends to exhibit higher base corner pressures than the permeable structures. For the permeable configurations, a reduction of approximately 30% in the base pressure is observed compared with the impermeable structures. This reduction is attributed to the ability of the pressure at the front base corner to dissipate beneath the crown wall in permeable structures. This pressure reduction is a localised effect and does not appear to significantly influence the horizontal force, provided that the wall height is sufficiently large.

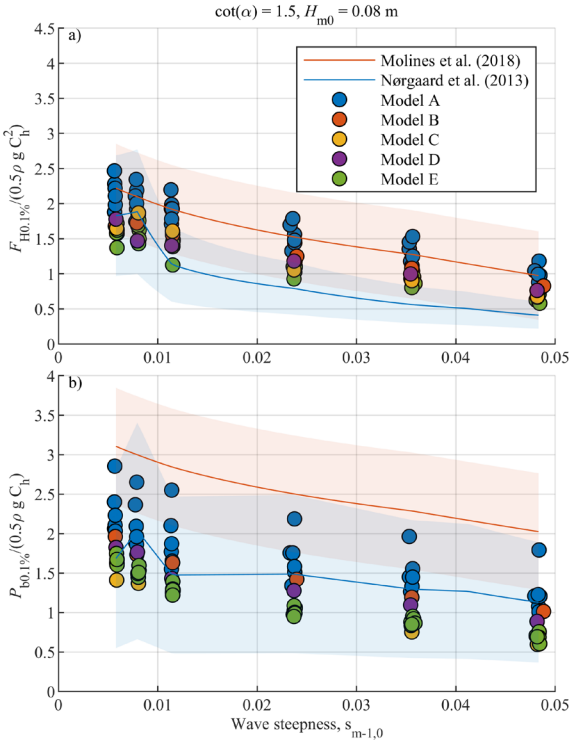


Figure 9. Influence of core permeability on horizontal force and base pressure for a fully protected wall with a 1:1.5 front slope. Identical wave trains are applied to all structures.

In terms of horizontal force prediction, the formulation by Molines et al. (2018) generally provides conservative estimates for the present dataset, whereas the formulation by Nørgaard et al. (2013) tends to be non-conservative. Conversely, for base pressure prediction, the formulation by Nørgaard et al. (2013) offers the most accurate representation, while the formulation by Molines et al. (2018) significantly overestimates the measured values. Overall, the results indicate that core permeability has a negligible influence on horizontal wave forces but may exert a modest effect on the pressure at the front base corner.

## 7 INFLUENCE OF PERMEABILITY WITH A PARTLY PROTECTED WALL

The influence of a partly protected crown wall is illustrated in Fig. 10. Notably, the prescribed 90% confidence bands associated with the formulation by Nørgaard et al. (2013) exhibit substantially greater uncertainty than those observed for the fully protected wall configuration, whereas the confidence bands prescribed by Molines et al. (2018) remain unchanged. The experimental data further indicate that Model A generally yields higher dimensionless load values. However, it should be noted that the wall height $C_h$ for this model is smaller than that of Models B and D. The difference between Models B and D is less pronounced than that observed for the fully protected wall case shown in Fig. 9. The relatively small variations observed for the partly protected wall are likely attributable to the reduced extent of the wall section influenced by rock armour placement, which in turn limits data variability. In contrast to the fully protected wall configuration, where the dimensionless horizontal force is nearly independent of wave steepness, the partly protected wall exhibits a clear dependence on wave steepness.

With respect to horizontal force prediction, the formulation by Molines et al. (2018) shows the best agreement with the experimental data for wave steepness values exceeding 0.02, whereas the formulation by Nørgaard et al. (2013) provides a more accurate representation for lower wave steepness. For the base pressure at the lower front corner, the formulation by Nørgaard et al. (2013) offers the most accurate description of the measured data, while the formulation by Molines et al. (2018) consistently overpredicts the pressure.

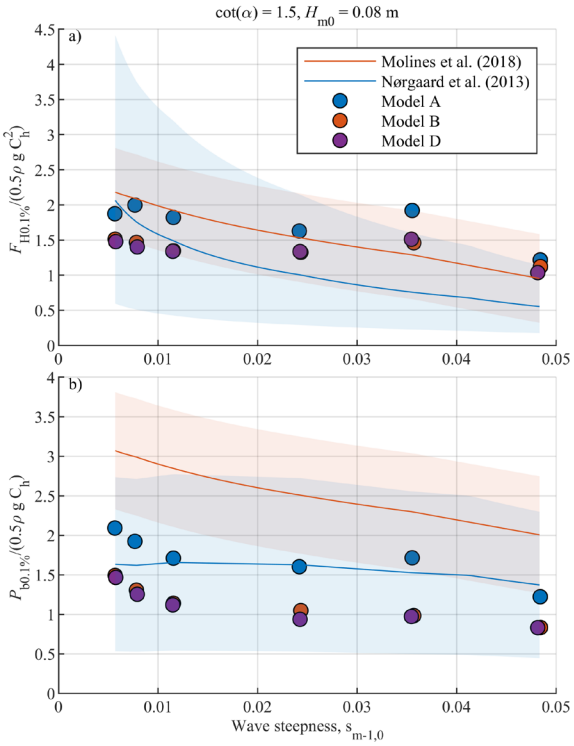


Figure 10. Influence of core permeability for a partly protected wall with a 1:1.5 front slope.

## 8 COMPARISON WITH EXISTING METHODS

Figure 11 presents a comparison between the measured dimensional loads and the corresponding predictions derived in the present study. The left-hand panels show predictions obtained using the formulation by Molines et al. (2018), while the right-hand panels present predictions based on Nørgaard et al. (2013). Panels (a) and (b) illustrate the horizontal force; panels (c) and (d) show the base pressure; panels (e) and (f) present the vertical force; and panels (g) and (h) depict the horizontal and vertical contributions to the overturning moment about the heel.

The prediction methods are evaluated using the following statistical indicators, where $P_i$ denotes the predicted value and $O_i$ the corresponding measured value:

$$MBE = \frac{1}{n}\sum_{i=1}^{n}(P_i - O_i)$$
$$\sigma_e = \sqrt{\frac{1}{n}\sum_{i=1}^{n}\left((P_i - O_i) - MBE\right)^2} \quad (6)$$
$$RMSE = \sqrt{MBE^2 + \sigma_e^2}$$

where MBE is the mean bias error, $\sigma_e$ is the standard deviation of the errors, and RMSE is the root mean square error. The MBE quantifies the systematic error of the predictions; a non-zero MBE indicates a biased model. The parameter $\sigma_e$ represents the random error and describes the scatter of the data, while RMSE reflects the total prediction error. The resulting statistical values are shown in Fig. 11.

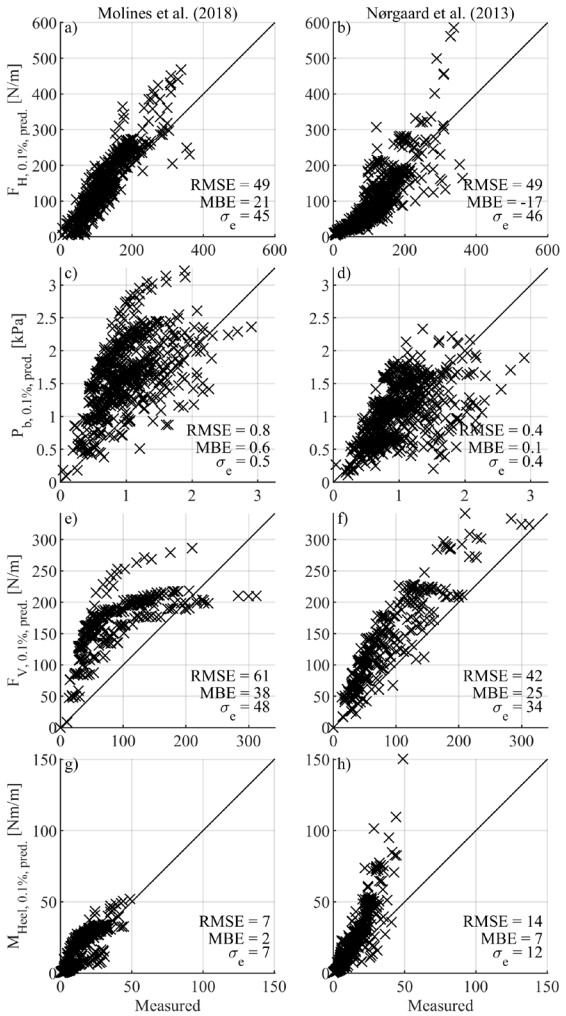


Figure 11. Comparison between measured forces and predicted values for all tested structures.

For the horizontal force, both prediction methods exhibit similar scatter and total error, as shown in Fig. 11. The primary difference lies in the bias: the formulation by Molines et al. (2018) shows a positive bias, whereas the formulation by Nørgaard et al. (2013) exhibits a negative bias.

For the base pressure, substantial scatter is observed for both methods. The formulation by Molines et al. (2018) displays a pronounced positive bias, resulting in a larger total error compared with the formulation by Nørgaard et al. (2013). Since the vertical force is assumed to follow a triangular pressure distribution and is strongly correlated with the base pressure, its prediction error reflects that observed for the base

pressure. Unlike the base pressure, the vertical force is absent for impermeable structures; these cases are therefore excluded from panels (e) and (f) of Fig. 11.

The total heel moment is best predicted by Molines et al. (2018), which exhibits the lowest scatter and total error. However, this apparent agreement results from an overestimation of the horizontal contribution combined with an underestimation of the vertical contribution. For impermeable structures (Fig. 12), where only the horizontal contribution to the moment is present, the formulation by Molines et al. (2018) underestimates the measured values (MBE < 0), whereas the formulation by Nørgaard et al. (2013) overestimates them.

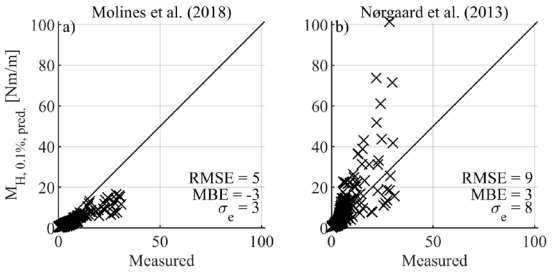


Figure 12. Comparison between measured horizontal contribution to the overturning moment and predicted values.

Table 6 summarises the ranges of parameters tested in the different experimental datasets. It is evident that the present dataset extends beyond, or deviates from, the ranges used to derive the formulae proposed by Molines et al. (2018) and Nørgaard et al. (2013). This discrepancy may partly explain the deviations observed between the measured values and the predictions in the present study.

Table 6. Tested parameter ranges for the different experimental datasets.

| Datasets | $\frac{H_{m0}}{L_{m-1,0}}$ | $\frac{H_{m0}}{h}$ | $\frac{h}{L_{m-1,0}}$ | $\frac{G_c}{L_{m-1,0}}$ | $\frac{R_c}{A_c}$ | $\frac{R_c}{H_{m0}}$ |
|---|---|---|---|---|---|---|
| Present data | 0.005-0.050 | 0.10-0.30 | 0.02-0.46 | 0.01-0.11 | 1.00-2.03 | 0.69-1.95 |
| Nørgaard et al. (2013) | 0.019-0.035 | 0.18-0.60 | 0.06-0.11 | 0.03-0.05 | 0.71-1.90 | 1.00-1.93 |
| Molines et al. (2018) | 0.011-0.061 | 0.14-0.32 | 0.04-0.37 | 0.01-0.08 | 1.06-2.39 | 1.32-2.88 |
| Pedersen (1996) | 0.016-0.071 | 0.16-0.35 | 0.08-0.32 | 0.03-0.19 | 1.00-2.64 | 0.61-3.63 |

## 9 CONCLUSIONS

This study extends the current understanding of wave-induced loads acting on crown walls by introducing a comprehensive experimental dataset that includes low wave steepness conditions and a wide range of structural permeabilities. The experimental results demonstrate that:

- Wave steepness has a significant influence on the measured loads, particularly for tests involving fully protected crown walls.
- Core permeability has a limited effect on horizontal wave forces but influences vertical forces and base pressures in permeable structures due to pressure dissipation beneath the crown wall.
- Existing empirical formulae remain broadly applicable, although their predictive accuracy varies depending on the load component and test conditions.
- The formulation proposed by Molines et al. (2018) provides the most accurate predictions of horizontal wave forces, albeit with a systematic positive bias. It also yields the best predictions of the total overturning moment; however, this apparent agreement results from an underestimation of the vertical moment combined with an overestimation of the horizontal moment.
- The formulation proposed by Nørgaard et al. (2013) offers more accurate estimates of base pressures and vertical forces.

Overall, the findings indicate that, while current design formulae are generally robust and the experimental data fall within the prescribed confidence bands, caution should be exercised when applying these methods to wave conditions outside the ranges for which they were originally developed. The new dataset provides valuable insight for the future refinement of design formulae, with the aim of improving guidance for structural safety assessments over a broader range of conditions. Until more reliable predictive methods become available, it is strongly recommended that crown wall designs be validated through physical model testing.

## ACKNOWLEDGEMENTS

This research did not receive any specific grant from funding agencies in the public, commercial, or not-for-profit sectors.

## 10 REFERENCES


Eldrup, M. R. & Lykke Andersen, T., 2019a. Applicability of Nonlinear Wavemaker Theory. *Journal of Marine Science and Engineering.*

Eldrup, M. R. & Lykke Andersen, T., 2019b. Estimation of Incident and Reflected Wave Trains in Highly Nonlinear Two-Dimensional Irregular Waves. *Journal of Waterway, Port, Coastal, and Ocean Engineering,* Volume 145.

Eldrup, M. R., Lykke Andersen, T. & Burcharth, H. F., 2019. Stability of rubble mound breakwaters—A study of the notional permeability factor, based on physical model tests. *Water.*

Eldrup, M. R., Lykke Andersen, T., Van Doorslaer, K. & Van der Meer, J., 2022. Improved Guidance on Roughness and Crest Width in Overtopping of Rubble Mound Structures Along EurOtop. *Coastal Engineering.*

Lamberti, A., Martinelli, L., Gabriella Gaeta, M., Tirindelli, M., Alderson, J., 2011. Experimental spatial correlation of wave loads on front decks. *Journal of Hydraulic Research* (49), 81–90.

Lykke Andersen, T., Clavero, M., Frigaard, P., Losada, M., & Puyol, J. I., 2016. A New Active Absorption System and its Performance to Linear and Non-Linear Waves. *Coastal Engineering,* Volume 114, pp. 47-60.

Lykke Andersen, T., Clavero, M., Eldrup, M. R., Frigaard, P. B., & Losada, M. 2018. Active Absorption of Nonlinear Irregular Waves. *Proceedings of the Coastal Engineering Conference*.

Martin, F. L., Losada, M. A. & Medina, R. J., 1999. Wave loads on rubble mound breakwater crown walls. *Coastal Engineering.*

Molines, J., 2016. Wave Overtopping and Crown Wall Stability of Cube and Cubipodarmored Mound Breakwaters. PhD Thesis. *Universitat Politècnica de València*.

Molines, J., Herrera P., M. & Medina R., J., 2018. Estimations of wave forces on crown walls based on wave overtopping rates. *Coastal Engineering.*

Nørgaard, J. Q. H., Lykke Andersen, T. & Burcharth, H. F., 2013. Wave loads on rubble mound breakwater crown walls in deep and shallow water wave conditions. *Coastal Engineering.*

Pedersen, J., 1996. Wave Forces and Overtopping on Crown Walls of Rubble Mound Breakwaters - An Experimental Study.

Schäffer, H. A., 1996. Second-Order Wavemaker Theory for Irregular Waves. *Ocean Engineering,* 23(1), pp. 47-88.

Tavakkol, S. & Lynett, P., 2017. Celeris: A GPU-accelerated open source software with a Boussinesq-type wave solver for real-time interactive simulation and visualization. *Computer Physics Communications,* Volume 217, pp. 117-127.

Van der Meer, J. W. 1988. Rock slopes and gravel beaches under wave attack. *Delft hydraulics*.

Van der Meer, J. W. & Stam, C. J. M., 1992. Wave runup on smooth and rock slopes of coastal structures. *Journal of waterway, Port, coastal, and Ocean Engineering.*

Zhang, H., Schäffer, H. A. & Jakobsen, K. P., 2007. Deterministic Combination of Numerical and Physical Coastal Wave Models. *Coastal Engineering,* 54(2), pp. 171-186.

Aalborg University, 2023a. *AwaSys - Software for Wave Laboratories.*
Available at: www.hydrosoft.civil.aau.dk/awasys

Aalborg University, 2023b. *WaveLab - Software for Wave Laboratories.*
Available at: www.hydrosoft.civil.aau.dk/wavelab